Microstructure tailoring for crack mitigation in CM247LC manufactured by powder bed fusion – Laser beam

Additive Manufacturing 99 (2025) 104672

Contents lists available at ScienceDirect

Additive Manufacturing

journal homepage: www.elsevier.com/locate/addma

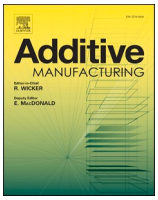

Microstructure tailoring for crack mitigation in CM247LC manufactured by powder bed fusion – Laser beam

Ahmed Fardan [a,*], Andrea Fazi [b], Jakob Schröder [c], Tatiana Mishurova [c], Tobias Deckers [d,e], Giovanni Bruno [c,f], Mattias Thuvander [b], Andreas Markström [g], Håkan Brodin [a,h], Eduard Hryha [a]

[a] Department of Industrial and Materials Science, Chalmers University of Technology, Göteborg 41296, Sweden
[b] Department of Physics, Chalmers University of Technology, Göteborg 41296, Sweden
[c] Bundesanstalt für Materialforschung und -Prüfung (BAM), Unter den Eichen 87, Berlin 12205, Germany
[d] Linde GmbH, Unterschleißheim 85716, Germany
[e] University Duisburg-Essen, Department of Manufacturing Technologies, Duisburg 47057, Germany
[f] University of Potsdam, Institute of Physics and Astronomy, Kalr-Liebknecht-Str.24-25, Potsdam 14476, Germany
[g] Thermo-Calc Software AB, Solna 16967, Sweden
[h] Siemens Energy AB, Finspång 61283, Sweden

ARTICLE INFO

Keywords:
Stripe width
Scanning strategy
Solidification cracking
CM247LC
Non-weldable superalloy
Residual stresses

ABSTRACT

Tailored microstructures in powder bed fusion – laser beam (PBF-LB) can aid in crack mitigation of non-weldable Ni-base superalloys such as CM247LC. This study explores the effect of a range of stripe widths from 5 mm down to 0.2 mm to control solidification cracking, microstructure, and residual stress in CM247LC manufactured by PBF-LB. The decrease in melt pool depth with the reduction in stripe width from 5 to 0.2 mm promoted the $<100>$ crystallographic texture along the build direction. The crack density measurements indicated that there is an increase from 0.62 mm/mm^2 (5 mm) to 1.71 mm/mm^2 (1 mm) followed by a decrease to 0.33 mm/mm^2 (0.2 mm). Atom probe tomography investigations at high-angle grain boundaries revealed that there is higher Hf segregation in 0.2 mm stripe width when compared to 5 mm. This indicates that the cracking behavior is likely influenced by the grain boundary segregation which in turn is dependent on melt pool shape/size and mushy zone length indicated by accompanying simulations. Residual stress, measured by X-ray diffraction, decreased from 842 MPa (5 mm) to 690 MPa (1 mm), followed by an abnormal rise to 842 MPa (0.7 mm) and 875 MPa (0.5 mm). This residual stress behavior is likely associated with the cracks acting as a stress relief mechanism. However, the 0.2 mm stripe width exhibited the lowest stress of 647 MPa, suggesting a different mechanism for stress relief, possibly due to re-melting. These findings highlight the critical role of stripe width as a scan strategy in PBF-LB processing of crack-susceptible alloys.

1. Introduction

Powder Bed Fusion – Laser Beam (PBF-LB) is one of the additive manufacturing (AM) processes where a three-dimensional (3D) part can be obtained from a digital file [1]. In PBF-LB, a laser beam melts powder particles layer-by-layer to manufacture a 3D part. The effect of different laser parameters such as laser power, speed, and hatch spacing has been explored widely for a plethora of materials. However, the scanning strategy has been less explored and can facilitate the manufacturing of difficult-to-process materials [2–5]. Certain Ni-base superalloys belong to this category as they undergo hot cracking (solidification and liquation cracking) during the PBF-LB process. Additionally, these alloys can be susceptible to solid-state cracking (ductility dip and strain age cracking) during post-processing heat treatment [6,7]. Both these types of cracking have rendered these alloys to be termed as 'non-weldable'. Most of the previous studies on non-weldable Ni-base superalloys have focused on minimizing hot cracking [8–13] but fewer studies have addressed solid-state cracking [14–16].

Hot cracking and solid-state cracking in PBF-LB can be minimized in different ways. Firstly, modification of the alloy composition to

* Corresponding author.
E-mail address: fardan@chalmers.se (A. Fardan).

https://doi.org/10.1016/j.addma.2025.104672
Received 3 July 2024; Received in revised form 17 December 2024; Accepted 23 January 2025
Available online 25 January 2025

minimize segregations and possibly γ' content can aid in reducing the cracking [10,11,17]. Secondly, development of completely new alloys with increased cracking resistance [7,17,18]. The increased developmental effort required for both approaches render such alloys unattractive to end users. The end users prefer to use 'heritage alloys' developed for traditional manufacturing techniques (such as conventional or directional solidification casting). Therefore, the final approach that can be used to facilitate defect-free PBF-LB components is to optimize the process parameters. Process optimization involving laser power, laser speed, and hatch spacing is not effective for these alloys [16]. However, modifying the scan strategies might aid in minimizing hot cracking. Lam et al. [19] explored different scan strategies to study the impact of hot cracking in IN738LC, which is a non-weldable Ni-base superalloy. It was found that a scan rotation of 90° gave lower crack density than the traditional 67° rotation. This was attributed to the observed reduction in the high-angle grain boundary (HAGB) fraction. Similar conclusions have been reached in another study [20]. This indicates that minimizing the HAGB fraction could be beneficial in reducing the hot cracking [12,19]. In addition to this, a recent study by Phan et al. [21] explored the impact of stripe widths of 5 and 10 mm on hot cracking in CM247LC. The study showed that stripe width of 5 mm led to lower hot cracking. The influence of stripe width on microstructure and residual stresses were not reported in the literature yet.

Residual stress (RS) from the PBF-LB process is also problematic. The high residual stress locked in the microstructure after production and the stresses arising from precipitation during the heat treatment, can lead to solid-state cracking. These cracks often occur in complex features like notches, which act as stress concentrators. In contrast to hot cracking, solid-state cracking poses a significant drawback as it leads to the formation of macro-cracks, often necessitating the scrapping of the printed part. Hilal et al. have shown that it is difficult to control both RS and hot cracking [22]. It has been revealed that having defects suc as lack of fusion porosities or more hot cracks could lead to lower RS values. However, this causes further complications as these defects cannot be eliminated during hot isostatic pressing. Therefore, it is of utmost importance to control hot cracking and residual stresses to fully harvest the benefits of AM for non-weldable Ni-base superalloys.

Therefore, in this study, an unexplored scanning strategy i.e. *stripe width* in the PBF-LB process. There have been very basic studies on the impact of stripe width in PBF-LB [23,24]. Also, the traditional stripe width employed in different publications ranges from 10 to 2.5 mm [23,25,26]. However, in our study, the stripe width has been varied from 5 to 0.2 mm for CM247LC, a non-weldable Ni-base superalloy. The reason for exploring stripe widths as low as 0.2 mm is to mimic spot-like melting that could modify the thermal gradients and in turn the microstructure and the residual stresses. The point (or spot) melting strategy has shown to be promising for powder bed fusion – electron beam (PBF-EB) to manufacture difficult-to-process materials [27,28]. To the authors' knowledge, this is the first study trying to implement such a strategy in PBF-LB. In this study, the samples obtained with different stripe widths (5–0.2 mm) have been systematically characterized for crack density, microstructure, residual stresses, and grain boundary segregation. Furthermore, simulations have been employed to obtain thermal history and information about the melt pool and the mushy zone. Our findings indicate that a short stripe width is effective in minimizing both hot cracking and residual stresses and in turn solid-state cracking. This result is expected to promote the utilization of PBF-LB of advanced non-weldable Ni-base alloys. Naturally, the point-like melting strategy could further be explored and developed for PBF-LB to manufacture difficult-to-process materials.

2. Methodology

2.1. Material

Gas atomized CM247LC with a particle size range of 15–45 μm was provided by Höganäs AB (Höganäs, Sweden) as feedstock material. The chemical composition of CM247LC powder as provided by the powder supplier and analysis performed on the printed PBF-LB part is provided in Table 1. Carbon and oxygen content were measured using combustion and fusion analysis, respectively. The remaining elements were measured using ICP-OES analysis.

2.2. Sample manufacturing

An EOS M290 PBF-LB machine was used to manufacture the parts. This machine operates a Yb-fiber laser with a maximum power of 400 W and a laser spot size of about 100 μm. The power (P), speed (v), hatch distance (h), and layer thickness (t) used for manufacturing were 200 W, 3000 mm/s, 0.03 mm, and 0.03 mm, respectively. These parameters were optimized in a dedicated process optimization carried out by the authors in a previous study [16]. A layer thickness (t) of 0.03 mm without build plate preheating was used. A stripe scan strategy was used where the cross-section to be exposed is divided into stripes of a certain width (known as 'stripe width') and bidirectional scan vectors expose one stripe at a time. The stripe width was varied as 5, 2.5, 1, 0.7, 0.5, and 0.2 mm, while the stripe overlap was fixed at 0.12 mm. The skywriting was switched on for all the samples. Skywriting is a common technique where the laser braking and acceleration regions are outside the exposure area when changing directions and aids in preventing the build-up of heat. It is to be also noted that an interlayer scan rotation of 67° was employed. The parts were removed from the build plate by electrical discharge machining (EDM).

2.3. Microstructural characterization

2.3.1. Sample preparation for OM and SEM

The cross-section parallel to the build direction was used for the microstructural investigations. The cross-sections were hot mounted in conductive bakelite resin and ground using SiC paper with 320, 500, 800, 1200, 2000 and 4000 grit-size on a Struers Tegrapol. This was followed by polishing using a diamond suspension of 3 μm on a taffeta woven wool surface (MD-Mol by Struers). A final 1 μm polishing was employed before optical microscopy (OM) measurements using Zeiss Axiovision 7.

The defect analysis consisted of acquiring a stitched image (~9.5 mm × 9.5 mm) along the build direction at a magnification of 100X on as-polished samples as shown in [29] followed by using the Fiji ImageJ software [30] for defect quantification. The region of interest is cropped and binarized. The 'Analyze Particle' function is applied to exclude border defects and particles smaller than 20 pixels. A circularity between 0 and 0.3 is identified as a crack. The individual crack length is acquired by obtaining the major axis length of the fitted ellipse. The sum of the individual crack length (in mm) divided by the analyzed cross-sectional area (in mm^2) gives the crack density. This measurement is repeated for all the samples for a total of 3 times after some grinding and polishing to obtain an average value with standard deviation.

The melt pool measurements were performed on OM micrographs on swab etched samples using Kalling's 2 (Water Kallings, 5 g $CuCl_2$ + 100 ml 37 % HCl + 100 ml ethanol) obtained at a magnification of 200X. In addition, electrolytic etching using 10 wt% phosphoric acid was performed using a voltage of 5–10 V for about 10–20 s to analyze the solidification structure by scanning electron microscopy (SEM).

2.3.2. SEM and EBSD acquisition

Before high resolution SEM analysis using a Leo Gemini 1550 SEM, the surface underwent a final polishing step using a 0.05 μm colloidal silica to remove any deformation caused by previous grinding/polishing. Electron Backscatter Diffraction (EBSD) acquisition was performed using a Leo Gemini 1550 SEM equipped with a Nordlys II detector. EBSD acquisition was performed using an accelerating voltage of 20 kV and an aperture size of 120 μm. A step size of 2 μm using an 8 × 8 camera mode

Table 1
Chemical composition of the CM247LC powder and the PBF-LB part (at% and wt%) used in this study.

		Cr	Co	Mo	C	W	Hf	Ta	Ti	Al	Zr	B	Si	O	Ni
Powder	at%	9.20	9.43	0.31	0.30	3.15	0.44	1.06	1.00	12.40	0.006	0.06	0.17	0.04	Bal.
	wt%	8	9.3	0.5	0.06	9.7	1.3	3.2	0.8	5.6	0.009	0.01	0.08	0.01	Bal.
PBF-LB part	at%	9.29	9.21	0.34	0.30	3.08	0.45	1.02	1.00	12.16	0.01	0.10	0.23	0.02	Bal.
	wt%	8.1	9.1	0.54	0.06	9.5	1.34	3.1	0.8	5.5	0.011	0.019	0.11	0.005	Bal.

with an exposure time of 7 ms (acquisition rate of ~50 Hz) was used for overall texture analysis at a magnification of 200X over an area of 800 μm x 800 μm. A basic clean-up consisting of removing wild spikes and zero solution removal using 7 nearest neighbors were employed. The EBSD maps and pole figures were plotted using the open source MTEX toolbox (version 5.9.0) [31] in MATLAB®.

The EBSD acquisitions for Kernel Average Misorientation (KAM) maps were obtained using a Leo Gemini 1550 SEM equipped with a Nordlys II detector. The acquisition was performed at an accelerating voltage of 20 kV and aperture size of 120 μm at a magnification of 10,000X. A step size of 0.0375 μm (37.5 nm) was used using a 4 × 4 camera mode with an exposure time of 11.6 ms (acquisition rate of ~40 Hz). The hit rates for the samples ranged from 99.4 % to 99.9 %, therefore, no clean-up tool was employed. The KAM maps and distributions were plotted using the open source MTEX toolbox (version 5.9.0) [31] in MATLAB®. The geometrically necessary dislocation (GND) density was obtained from the EBSD data.

Large Area Mapping (LAM) EBSD acquisitions were performed using a Zeiss Gemini 450 SEM equipped with an Oxford Symmetry detector (Oxford Instruments, Abingdon, Oxfordshire, England) at an accelerating voltage of 20 kV and a probe current of 10 nA. The large area acquisition was done at a magnification of 150 X with a step size of 3 μm and acquisition rate of ~3000 Hz. Basic clean up consisting of removing wild spikes and zero solution removal ranging from 8 to 5 nearest neighbors were employed. The EBSD maps were processed and plotted using Aztec Crystal.

2.3.3. ECCI and total dislocation density measurement

Electron Channeling Contrast Imaging (ECCI) was performed using the Zeiss Gemini 450 SEM on samples polished with colloidal silica. ECCI acquisition was performed using a 6-sector backscattered electron detector at 20 kV accelerating voltage, 1.5 nA probe current and a working distance of ~5 mm. Unlike controlled ECCI (cECCI), this technique does not use EBSD orientation information to guide the rotation and tilt to achieve the channeling conditions [32]. Therefore, the ECCI acquisitions were performed at a 0° tilt angle on a region that appears dark, i.e. nearly in channeling conditions. The presence of carbides could also be seen in addition to the dislocations due to the Z-contrast (Z = atomic number). Unlike KAM which reveals only GND, ECCI reveals both SSD (statistically stored dislocations) and GND.

Dislocation density measurements were performed using the Fiji ImageJ software [30] on images acquired at a magnification of 50,000X (pixel size ~2 nm) at low scan speeds. The Trainable Weka Segmentation plugin [33] within the Fiji ImageJ software was used to classify the matrix, carbides and dislocations. This was followed by applying a threshold followed by using the 'Analyze Particle' function to count the number of dislocations. The threshold was kept at 15 % constant for all the images. This was then divided by the area of the image in m^2 to obtain the dislocation density (in m^{-2}).

Dislocation density measurements from ECCI have not yet been proven fully quantitatively reliable. A study comparing measurements through ECCI and transmission electron microscopy (TEM) showed that two times lower dislocation density was obtained in ECCI [34]. Nevertheless, the dislocation density measured from ECCI in this study is for comparative purposes.

2.4. Atom probe tomography (APT) analysis

The atom probe measurements were performed using a local electrode atom probe LEAP 6000 XR from CAMECA. The instrument was used in laser pulse mode at 50 K specimen temperature, 0.5–1.0 % evaporation rate, and 30–35 pJ laser energy. Auto pulse frequency control was implemented and set to guarantee a minimum mass spectrum range of 180 Da. All APT specimens were obtained from polished cross-sections of bakelite embedded samples with a focused ion beam/SEM dual-beam FEI Versa 3D workstation implementing well-known lift-out procedures [35]. This workstation was equipped with a backscattered electron detector, which was utilized to pinpoint the grain boundary locations, making it possible to ensure that the examined grain boundaries were included in the measurement volume. The CAMECA APT Suite 6.3 software was used for data reconstruction and data evaluation.

2.5. Residual stress measurements

Subsurface residual stress analysis was conducted on the laboratory energy dispersive diffractometer LIMAX-160 at Helmholtz Zentrum Berlin, Germany. The basis for the generation of X-rays on this diffractometer is a MetalJet source from Excillum (Model D2), featuring a liquid Ga-rich alloy as anode material. Since the anode flows continuously, it is possible to work with a high electron density even at high acceleration voltages and, in this way, generate a source with a small size and a significantly higher photon flux compared to conventional X-ray tubes. The LIMAX-160 instrument allows acceleration voltages up to 160 kV. A polycapillary primary optic with a circular collimator of 1 mm was used.

The center point at the lateral specimen surface was measured. Before the experiment, the surface was locally electropolished to remove around 50 μm of material to avoid the effect of surface roughness on the measurements using an ATM Kristall 650. The $sin^2\psi$ method was used to determine the subsurface residual stress of the 311 peak in reflection mode at a fixed diffraction angle of 16°. This results in a penetration depth of approximately $\tau_0 \approx 20$ μm. The residual stress in the building direction (BD) and in the transversal direction (TD) were measured. The EDDIDAT (Energy-Dispersive Diffraction Data Analysis Tool) software was used for diffraction peak fitting and residual stress calculation [36]. The X-ray diffraction elastic constants (DEC) were calculated according to the Reuss model using ISODEC [37]: $s_1 = -1.436 \times 10^{-6}$ MPa^{-1} and $\frac{1}{2}s_2 = 6.955 \times 10^{-6}$ MPa^{-1} using single crystal elastic constants for CM247LC reported in [38].

2.6. Simulation of PBF-LB process

The Additive Manufacturing Module in Thermo-Calc 2024a was utilized to simulate the PBF-LB process. The composition used for the simulation is shown in Table A1 in Appendix A1. Appendix A2 contains a brief overview of equations used to model the PBF-LB process [39]. The TCNI12 database was employed for Scheil solidification calculations. A transient simulation was done using a calibrated Gaussian heat source. The calibrated heat source had an absorptivity of 70 % and a beam diameter of ~80 μm. The top boundary condition had a radiation emissivity of 0.8 and a convective heat transfer coefficient of 20 W/m^2. Evaporation was considered in the simulations. The laser power, speed

and hatch were 200 W, 3000 mm/s and 0.03 mm, respectively. The layer thickness used was 30 μm. The simulation was performed for one layer using a bi-directional scan strategy. The simulation geometry had a margin of 0.1 mm and a width of 0.7 mm which led to having 17 scan tracks. The length of the geometry varied based on the stripe width simulations performed. In this study, simulations were performed for all the stripe widths used in the experiments. However, only the results for the 0.2 mm and 5 mm stripe width will be presented. No lift time (corresponding to skywriting) was considered between the single tracks. Fluid-flow including Marangoni effect was also not considered and the material properties of the powder is assumed to be the same as the bulk material.

3. Results

3.1. Defect formation and melt pool characteristics

The representative OM images in Fig. 1. show that there are changes in the cracking with the decrease in stripe width. The cracking is seen to increase when the stripe width is decreased from 5 mm to 1 mm. However, the cracking reduces as the stripe width is further decreased from 1 mm to 0.2 mm. The average crack density is shown in Fig. 1 (top right in mm/mm^2) and plotted in Fig. 2**a** as per Section 2.3. The average crack density was measured to be 0.62 mm/mm^2 for 5 mm stripe width, which then increased to 1.71 mm/mm^2 as the stripe width decreased to 1 mm. This was then followed by the lowest crack density of 0.33 mm/mm^2 for a stripe width of 0.2 mm.

The melt pool depth was obtained from the top layer of etched micrographs for different stripe widths and is depicted in Fig. 2b. It can be observed from Fig. 2b that there is a decrease in the melt pool depth from about 53 μm for 5 mm stripe width to 38 μm for 0.2 mm stripe width. The differences in the crack density observed in Fig. 1 and Fig. 2a are most likely caused by the changes in the energy input and hence melt pool depth. The differences in energy input were confirmed based on melt pool monitoring (MPM) data obtained during the PBF-LB using various stripe widths, see Fig. 3. The color bar in Fig. 3 refers to the emitted melt pool radiation, intensity, which is equivalent to the relative energy input into the material. The average and standard deviation of the MPM intensity has been tabulated in Table B1 in Appendix B. MPM has a spatial resolution of ~50–100 μm, which is suitable for observing phenomena occurring at the melt pool and even more suitable on the stripe width scale. From Fig. 3, it can be visually observed that the stripe width reduces from Fig. 3a to f. The lower intensity observed in the stripe overlap region probably arises from the skywriting process employed within the PBF-LB process. The laser switches on/off at the beginning and the end of the melt pool track, creating larger time delays between each of the scans and hence scan vectors, therefore leading to a lower energy input to the material. Therefore, by reducing the stripe width to 0.2 mm (Fig. 3f), the energy input decreases so that shallower melt pools are observed (Fig. 2b). The average MPM intensity measured reduced from ~6500 to 6000 as the stripe width is reduced from 5 to 0.2 mm. This is a unique way of modifying the energy input to the material despite having the same laser parameters (power, speed, and hatch) and could possibly also reduce the cracking susceptibility of the so called non-weldable Ni-base superalloy CM247LC.

3.2. Microstructural characterization by SEM, EBSD, and ECCI

3.2.1. Solidification structure

The SEM images recorded on etched microstructures (Fig. 4) indicate that the solidification structures are different for samples built with stripe widths of 5 mm and 0.2 mm. In Fig. 4a, b, it can be observed that the solidfication structures for samples built with stripe width of 5 mm have different orientations due to differences in thermal gradient. This can be also seen by a slightly deeper melt pool (~53 μm). The solidification structures are columnar and oriented nearly parallel to the build direction for the sample built with a stripe width of 0.2 mm (Fig. 4c, d). This can be attributed to the shallower melt pool (~38 μm) achieved for a stripe width of 0.2 mm.

Observing the crack vicinity showed that the cracks were found mostly in regions where there was certain degree of misorientation between the solidification structures i.e. grain boundaries. This can be clearly seen in Fig. 5a for the sample built with a stripe width of 5 mm. The insert Fig. 5b also shows the evidence of the solidification structure within the crack proving that the cracks observed were primarily solidification cracking. Although it was shown that the solidification structures were oriented parallel to the build direction for the stripe width of 0.2 mm, there were also some solidification cracks observed (shown in Fig. 5c, d).

3.2.2. Texture and grain characteristics

The impact of the stripe width on the grain morphology and texture is shown in the EBSD orientation-maps in inverse pole figure (IPF) representation in Fig. 6. A common observation is that the samples with different stripe widths have a strong < 100 > texture as observed from the (100) pole figure. However, the intensity of the < 100 > texture is affected by the stripe width. The < 100 > intensity in MRD increases from ~4 to 12 as the stripe width decreases from 5 to 0.2 mm. This is

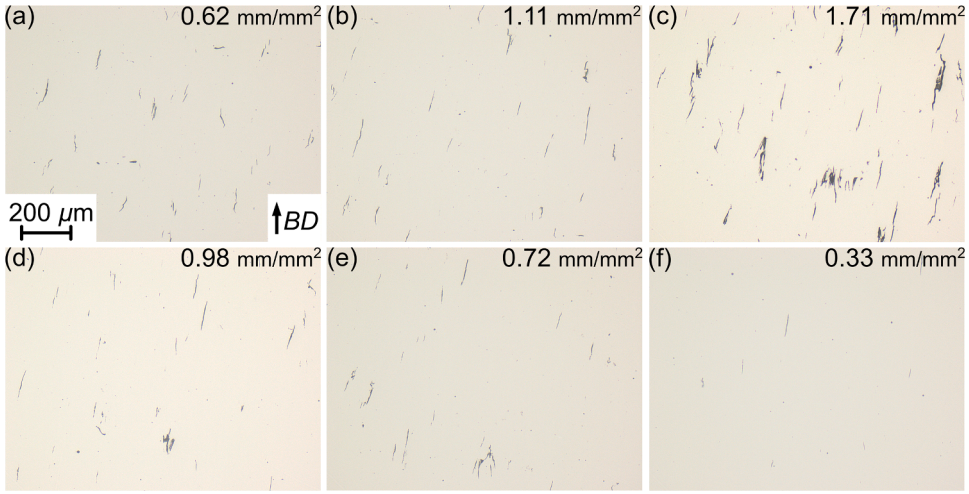

Fig. 1. OM images of the samples for stripe widths of (a) 5 mm, (b) 2.5 mm, (c) 1 mm, (d) 0.7 mm, (e) 0.5 mm and (f) 0.2 mm. All the images have the same scale as shown in (a) and crack densities (in mm/mm^2) are indicated in the top right corners.

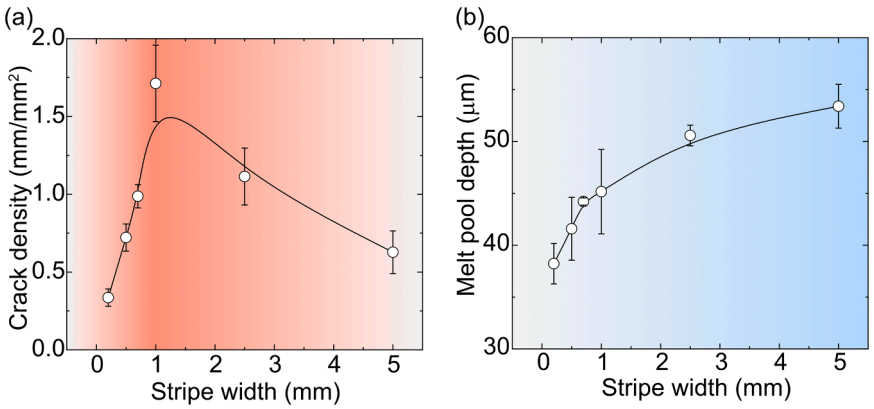

Fig. 2. (a) Crack density measurements obtained from polished OM micrographs, (b) Melt pool depth measurements obtained from etched OM micrographs. Error bars indicate the standard deviation from three measurements for a given condition.

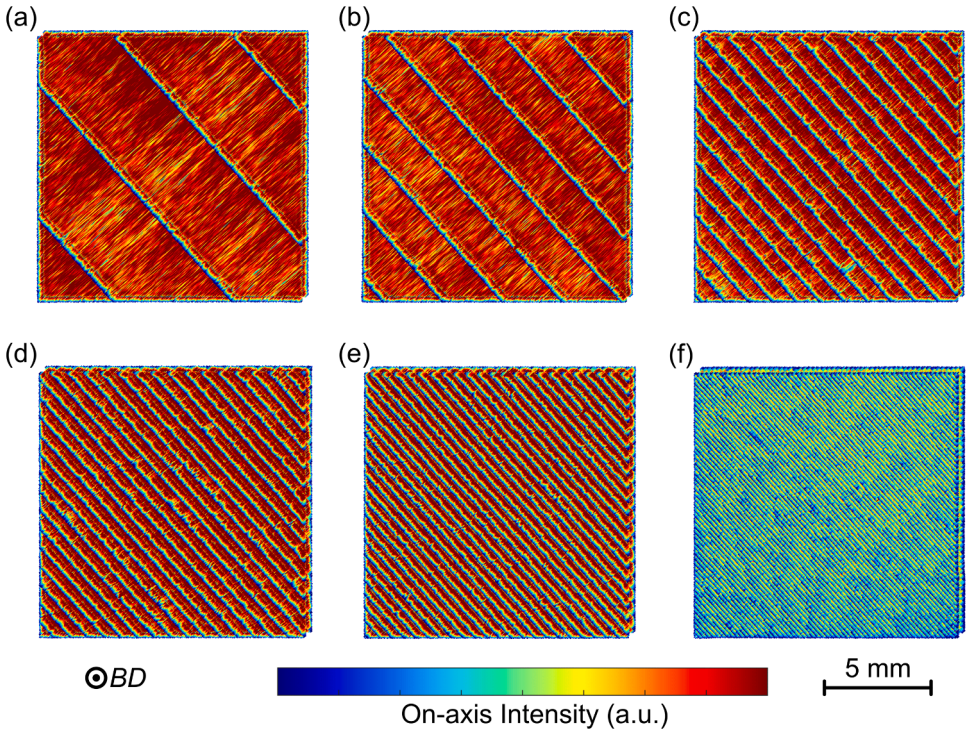

Fig. 3. Melt pool monitoring (MPM) data of samples built with stripe widths of (a) 5 mm, (b) 2.5 mm, (c) 1 mm, (d) 0.7 mm, (e) 0.5 mm and (f) 0.2 mm. The on-axis Intensity (in arbitrary units) refers to the relative energy input to the material.

also seen in the orientation-maps where the 5 mm stripe width has fine equiaxed and columnar grains as observed in the IPF map in Fig. 6a. As the stripe width is reduced to 1 mm (Fig. 6c), there is a transition to a columnar-like microstructure. A further decrease in stripe width from 1 to 0.2 mm (Fig. 6d-f) leads to a distinct columnar microstructure. This change from equiaxed to columnar microstructure with the reduction of the stripe width can be attributed to the changes in melt pool depth and hence geometry. The melt pool depth decreased with the decrease in stripe width from 5 to 0.2 mm (Fig. 2b). From the supplementary figure Fig. C1 in Appendix C, it is seen that there is a decrease in fraction of HAGB where misorientation is greater than 10° as the stripe width is reduced from 5 to 0.2 mm. Subsequently, there is an increase in the low angle grain boundaries (LAGB) where misorientation is between 2° and 10°. This is also tabulated in Table C1 in Appendix C, which shows that the HAGB fraction decreases from 55 % to 33 % and the LAGB fraction increases from 45 % to 67 % as the stripe width is decreased from 5 to 0.2 mm.

3.2.3. *Characterization of dislocation structures by EBSD and ECCI*

EBSD was performed to analyze the KAM distribution for the different stripe widths (see Fig. D1 in Appendix D). The GND density was obtained using similar parameters from the EBSD data and the value was similar for all the stripe widths at approximately 40×10^{14} m^{-2}. Therefore, ECCI was performed to measure the total dislocation density. ECCI images in Fig. 7 show differences in appearance and density of dislocations. The presence of dislocations within cellular structures were found (SSDs) in addition to some dislocations in the cellular boundaries (GNDs). Additionally, carbides could also be observed due to the Z-contrast. The carbides are primarily observed along the cell boundaries of the cellular structures. The carbides observed in Fig. 7f for 0.2 mm stripe width appear to be coarser than in other samples (Fig. 7a-e).

A more equiaxed cellular structure is observed for the 5 mm stripe width sample, see Fig. 7a. The same can also be observed in Fig. D1a in Appendix D. However, for lower stripe widths of 2.5–0.2 mm there is a presence of columnar cellular structures. The dislocation arrangement

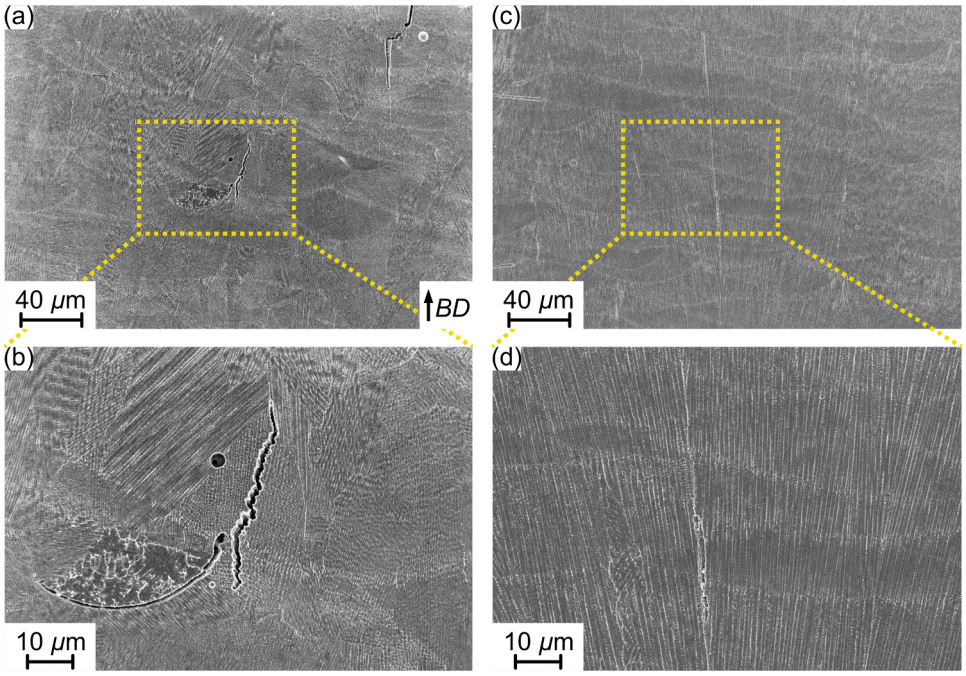

Fig. 4. SEM images of etched samples showing cellular structures of samples built with stripe width of (a) 5 mm and (c) 0.2 mm. (b) and (d) are magnified images of the areas marked in (a) and (b), respectively.

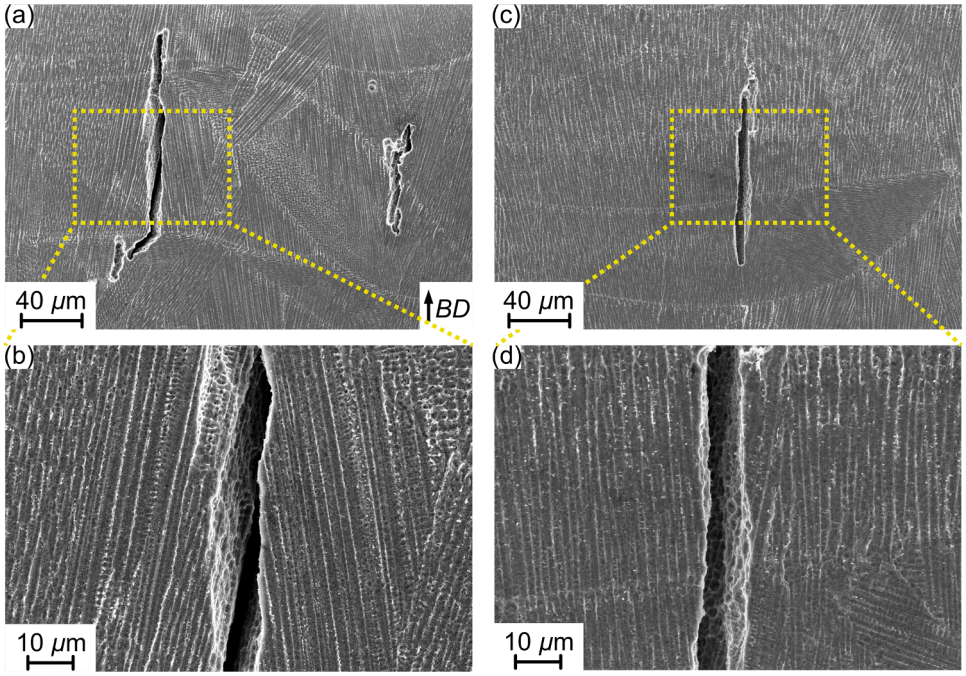

Fig. 5. SEM images of etched samples showing solidification structure and solidification crack surfaces of samples built with stripe width of (a) 5 mm and (c) 0.2 mm. (b) and (d) are inserts marked in (a) and (c), respectively.

also appeared to have been affected by the stripe width. For 5 mm stripe width, it is observed that there are some dislocations in the bulk of the cellular structures i.e. SSDs (Fig. 7a). But it can also be seen that the dislocations in the cellular boundaries i.e. GNDs, cannot be clearly observed from ECCI (Fig. 7a). However, from Fig. 7b-f, dislocations are much more clearly observed and appear to be primarily SSD from ECCI. In general, the bright regions around carbides near cell boundaries were observed, that could probably be dense dislocation networks (GND). The total dislocation density measured from the ECCI is found to increase from 3.7×10^{14} to 8.5×10^{14} m^{-2} as the stripe width is decreased from 5 to 0.5 mm (see Table 2). This is followed by a decrease in the total dislocation density to 4.8×10^{14} m^{-2} for the 0.2 mm stripe width.

3.3. Residual stress analysis

Fig. 8 shows the residual stress values in the BD and TD for the samples with different stripe widths. A general observation is that the BD and TD residual stress profiles are similar. However, at the lateral

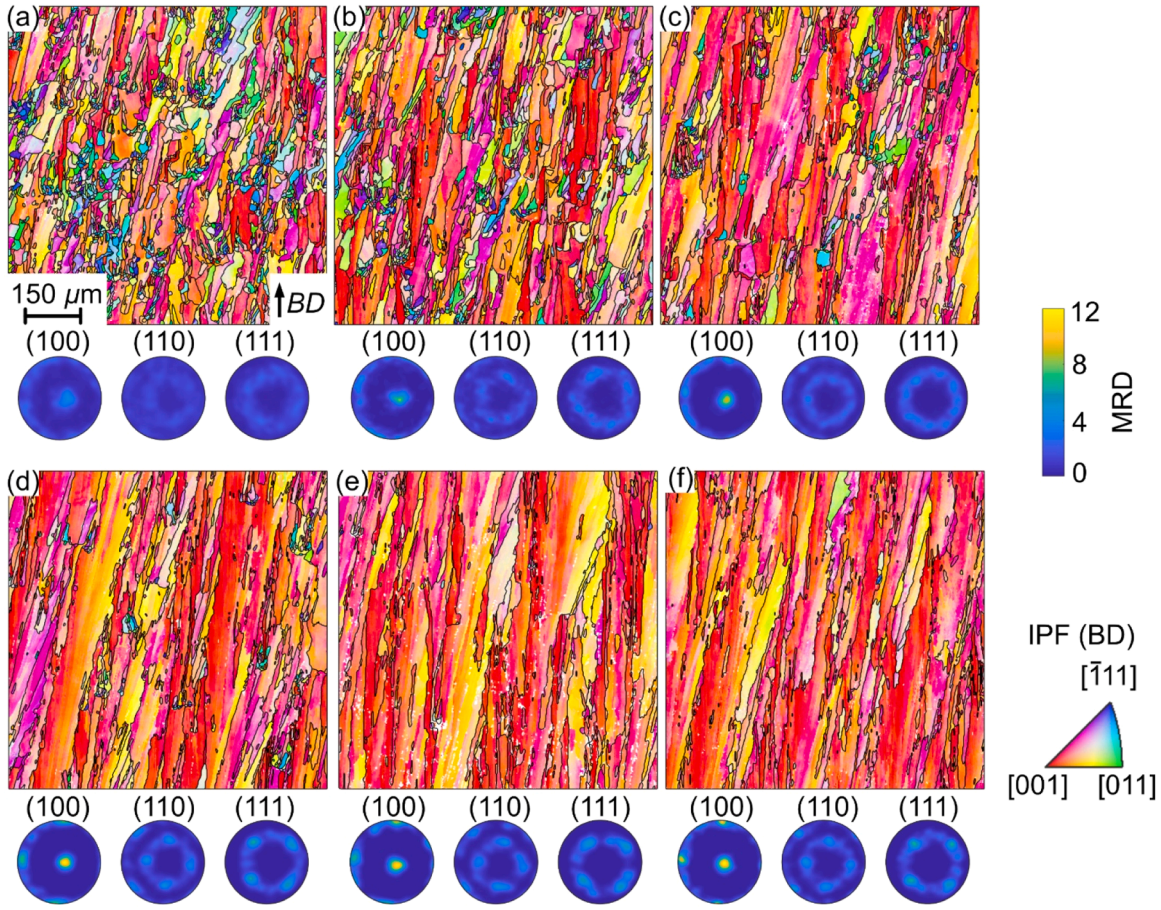

Fig. 6. EBSD orientation maps in IPF representation and the corresponding pole figures for stripe widths of (a) 5 mm, (b) 2.5 mm, (c) 1 mm, (d) 0.7 mm, (e) 0.5 mm and (f) 0.2 mm. The orientation maps are shown along build direction (BD) and the IPF coloring is along the BD. All the EBSD maps have the same scale. The pole figure intensity is represented as multiples of random distribution (MRD).

surface the BD residual stress values are much higher, as typical for PBF-LB materials (especially in the subsurface region) [40]. The TD residual stress values are in the range of approximately 200 – 400 MPa, while the BD residual stress values range between 600 – 900 MPa. Therefore, the BD residual stress values will be the focus from here on. The BD residual stress decreased from 850 MPa to 700 MPa as the stripe width was reduced from 5 mm and 1 mm (Fig. 8). Following this, the abnormal increase in the residual stress (~850–870 MPa) for 0.7 and 0.5 mm stripe width was observed. The lowest residual stress was obtained for 0.2 mm stripe width (~650 MPa).

3.4. Analysis of grain boundary segregation by APT

Site-specific APT samples were prepared from a random grain boundary (GB) for samples manufactured using 5 mm and 0.2 mm stripe width. Owing to the complexity of the grain boundaries in samples prepared using PBF-LB, only certain APT needles were successfully prepared containing the grain boundary. Furthermore, the execution of grain boundary samples in APT posed challenges due to the fractures occurring during the APT acquisition process.

The APT reconstruction of the sample manufactured with 5 mm stripe width is shown in Fig. 9a,b. One-dimensional (1-D) composition profiles (Fig. 10 a,c,e) were obtained across the grain boundary indicated by arrow 1 in Fig. 9a. The GB is delineated by isosurfaces of B and Hf in Fig. 9a,b. Higher and lower concentration limits are chosen to show the differences in segregation in and nearby the GB. B segregation is shown by 2.5 at% (dark blue) and 1 at% B (transparent blue) in Fig. 9a,c, while Hf segregation is shown with 6 at% (gold) and 1.5 at% (light yellow) in Fig. 9b,d. From the 1D compositional profile (Fig. 10 a, c,e), it is clear that B and Hf segregate to the GB, up to 0.80 and 3.0 at%, respectively. On the other hand, there appears to be a depletion of Cr and Co in the GB with values of 8.4 and 8.8 at%, respectively. While elements such as Al, W, Ti, Ta, and Mo indicate no clear segregation, as observed in Fig. 10 a,c,e. C and Si are observed to be segregating at the GB, up to 0.50 and 0.65 at%, respectively. Fig. 9a also shows a carbide, which is indicated by an isosurface of 10 at% C. There also appears to be some B segregation engulfing the carbide (indicated by 2.5 at% B) that can be observed in Fig. 9a. Fig. 10 shows a 1D compositional profile that was obtained across a carbide (arrow 2) shown in Fig. 9a. The carbide appears to be an MC-type carbide enriched in Hf, Ti, Ta, and W up to 8.0 at%, 12.2 at%, 13.5 at% and 11.1 at%, respectively, along with C enrichment up to 29 at% in the carbide (Fig. 11a). B and Si also appear to be segregating towards the carbide up to 0.79 at% and 0.97 at%, respectively.

The APT reconstruction of the sample manufactured with 0.2 mm stripe width is shown in Fig. 9c,d along with the 1-D compositional profiles (Fig. 10b,d,f) across the grain boundary indicated by arrow 3 in Fig. 9c. Similar to the finding for 5 mm stripe width (Fig. 10a,c,e), B and Hf segregate at the GB up to 1.4 at% and 3.4 at%, respectively. For the 0.2 mm stripe width, the GB appears to be enriched in Cr up to 13.2 at% and Co is constant at about 10.2 at%. Similar to the 5 mm stripe width, there seems to be segregation of C and Si up to 0.8 and 0.92 at%, respectively. There also appears to be a zone adjacent to the GB where there is segregation of the GB elements. This zone will be referred to as the 'enriched zone' in the 1-D compositional profiles shown in Fig. 10. This enriched zone tends to have segregations lower or higher than at

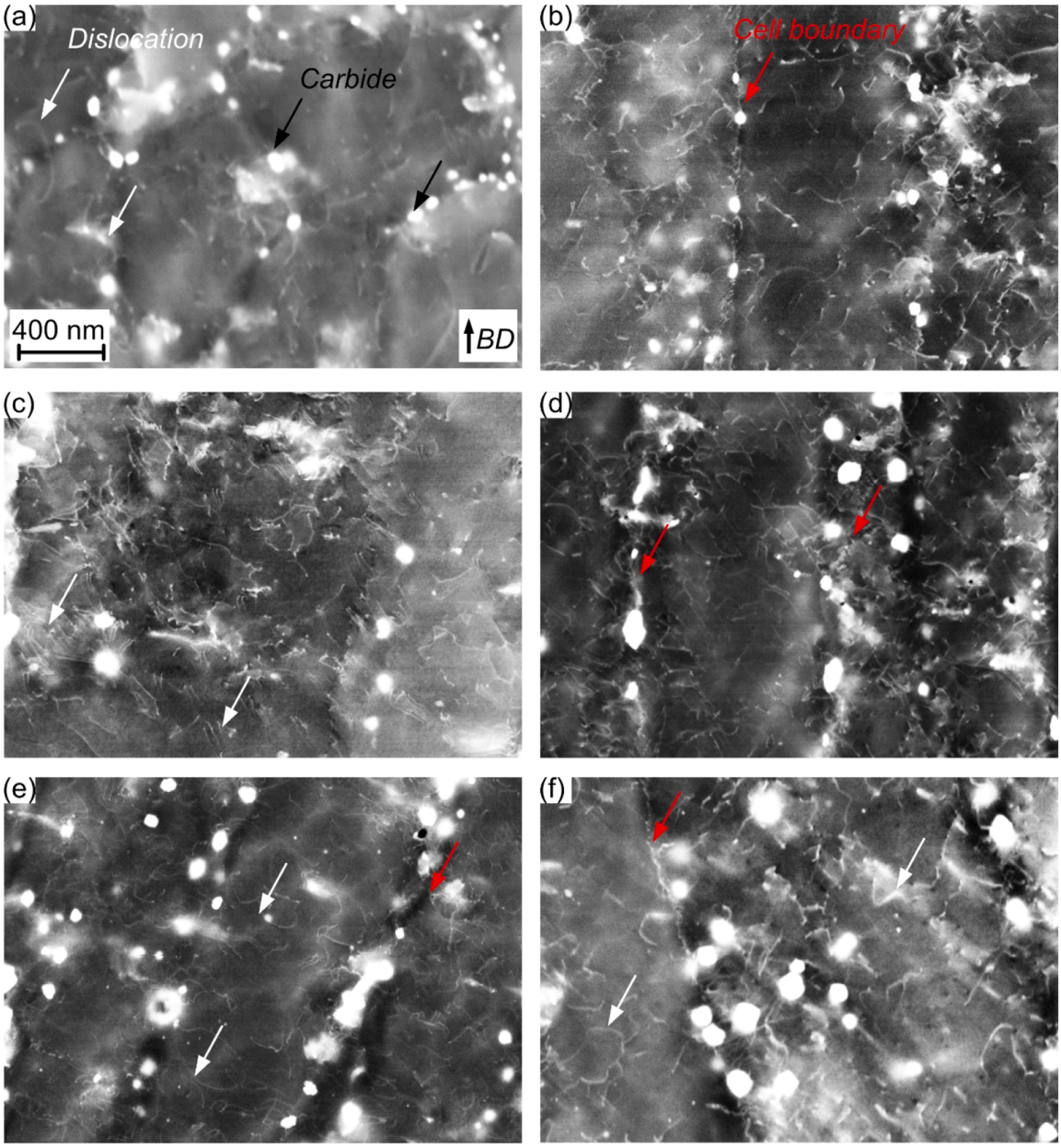

Fig. 7. ECCI of samples manufactured with different stripe widths showing dislocations, carbides and solidification structures. (a) 5 mm, (b) 2.5 mm, (c) 1 mm, (d) 0.7 mm, (e) 0.5 mm and (f) 0.2 mm.

Table 2
Dislocation density measurements for samples manufactured with different stripe widths.

Stripe width (mm)	5	2.5	1	0.7	0.5	0.2
Dislocation density ($\times 10^{14}$ m^{-2})	3.7	3.9	4.8	5.8	8.5	4.8

the GB. Such 'enriched zones' have previously been observed in [10,41] and were attributed to strong partitioning of certain elements in the residual liquid.

3.5. Process simulation

The simulation results for the standard process (5 mm stripe width) and the modified process (0.2 mm stripe width) are shown in Fig. 12. The melt pool plots shown in Fig. 12a, c are from a single layer multi-track simulation. The melt pool plots are shown by using isosurfaces to represent the solidus (Tsolidus) and the liquidus (Tliquidus) temperatures in Fig. 12 a,c. It is evident that the short stripe width leads to smaller melt pools and mushy zones for the modified process, i.e. with 0.2 mm stripe width (Fig. 12c). Such a decrease in the length of the melt pool + mushy zone could possibly be effective in reducing the solidification cracking as per the hot cracking criterion [42].

A three-dimensional view of the melt pool and the mushy zone is shown in Fig. A1 in Appendix A3. It is observed that the length of the mushy zone is 0.60 mm for 5 mm stripe width. The simulated mushy zone length then increases to 0.95 mm as the stripe width decreases to 2.5 mm with a further increase of the mushy zone length to 1.06 for a stripe width of 1 mm. With decreasing stripe width below 1 mm, the mushy zone starts to decrease. The simulated lengths of the mushy zone were 0.77 mm, 0.56 mm, and 0.29 mm for stripe widths of 0.7, 0.5, and 0.2 mm, respectively. The temperature profiles were also extracted from the start of the melt pool tracks for the first and the last tracks from the simulations. This was done to show the differences in the local

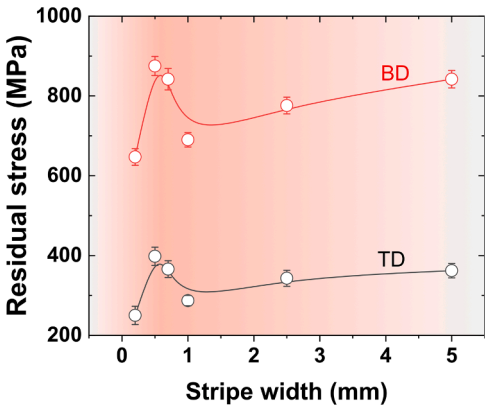

Fig. 8. Variation of residual stress with stripe width. BD and TD are residual stresses in build direction and transverse direction, respectively. Error bars correspond to the standard deviation 2σ.

temperature profiles, which could otherwise not be obtained experimentally. From Fig. 12 b,d, it can be observed that the time is shorter (note the different scales on the x-axis). Another observation is that the peak temperature difference between the two probed tracks is smaller for the modified process. This is indicated by the red and blue points in Fig. 12 b,d.

4. Discussion

This study demonstrates that the stripe width has a profound effect on solidification cracking, microstructure, and residual stress. Table 3 summarizes some of the key results.

The decrease in stripe width from 5 mm to 0.2 mm leads to a 46 % decrease in solidification cracking (crack density) that is attributed to the 28 % decrease in melt pool depth and 50 % decrease in the mushy zone length. There are some variations in crack density between stripe widths of 5 and 0.2 mm (see Table 3) that can be correlated with the mushy zone length and melt pool shape from process simulations. From Table 3, the crack density is proportional to the mushy zone length. Solidification cracks are known to occur in mushy zones in welding and PBF-LB [42,43]. This is due to the insufficient liquid feeding towards the end of the solidification in a brittle temperature range. According to Clyne and Davies [44], this range is when the solid fraction is between 0.9 and 0.99. Another observation from the simulation (Fig. A1 in Appendix A3) is that the mushy zone has a teardrop shape for 5 and 2.5 mm stripe width. The teardrop shape in welding is susceptible to solidification cracking due to the lower liquid feeding [45,46]. In such cases, using lower energy input and slower speeds (leading to shallower melt pools with elliptical shape) minimizes solidification cracking. Therefore, it is crucial to bear in mind the changes in the melt pool size/shape and mushy zone length when varying stripe width in PBF-LB for alloys susceptible to solidification cracking. Additionally, Phan et al. [21] have indicated through thermal imaging that there is a local enhancement of heat accumulation during the PBF-LB process of CM247LC with a reduction of stripe width from 10 mm to 5 mm. The authors claimed that this enhancement led to reduced thermal gradients. This experimental finding agrees with the crack density measurements and the process simulation from this study.

Here, we would also like to briefly mention that there are some discrepancies between the simulation and the experimental observations. One thing that we would like to point out is that from experiments we noticed a decrease in melt pool depth (Table 3) when comparing stripe widths of 5 and 0.2 mm. However, simulations indicate that we have a deeper melt pool for the 0.2 mm stripe width. This discrepancy arises from the assumptions we have made for the simulations regarding the heat source calibration, lift time (skywriting) and properties of powder and bulk. Such assumptions were important to minimize the computation time but led to a simulation that does not properly reflect the experiment. This shows that there is room for improvement especially in the numerical simulations to properly reflect the experimental observations.

The decrease in melt pool depth could also have an impact on the solidified cellular microstructure. The change in the solidified cellular structure for 5 mm and 0.2 mm stripe widths observed in Fig. 4 is attributed to the changes in the melt pool geometry. This geometry change can lead to a change in the direction of growth of the cellular structures within a melt pool [47,48]. During the solidification of the melt pool, the solidification structures grow perpendicularly to the melt pool boundary as it is the direction of the maximum thermal gradient and the maximum heat extraction. Hence, the solidification structures tend to grow in the preferential growth direction, which is < 100 > for alloys with face centered cubic crystal structures [49]. Therefore, for a deeper and narrower melt pool, the solidification structures can grow from the sides to the center, while for a shallower melt pool, the cellular structures solidify nearly parallel to the building direction [48]. Such

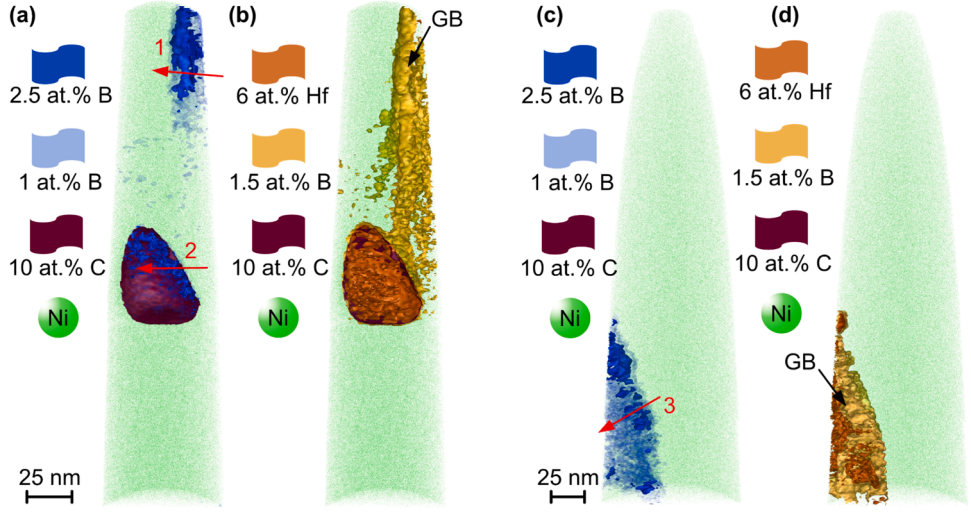

Fig. 9. (a), (b) Atom probe reconstruction of a random HAGB from the sample manufactured with 5 mm stripe width. (c), (d) Atom probe reconstruction of a random HAGB from the sample manufactured with 0.2 mm stripe width. GB refers to the grain boundary. Ni is presented as atoms in the APT needle. Isosurfaces of specific concentrations of B and Hf are used to show the GB region. Carbide is presented with isosurface of C.

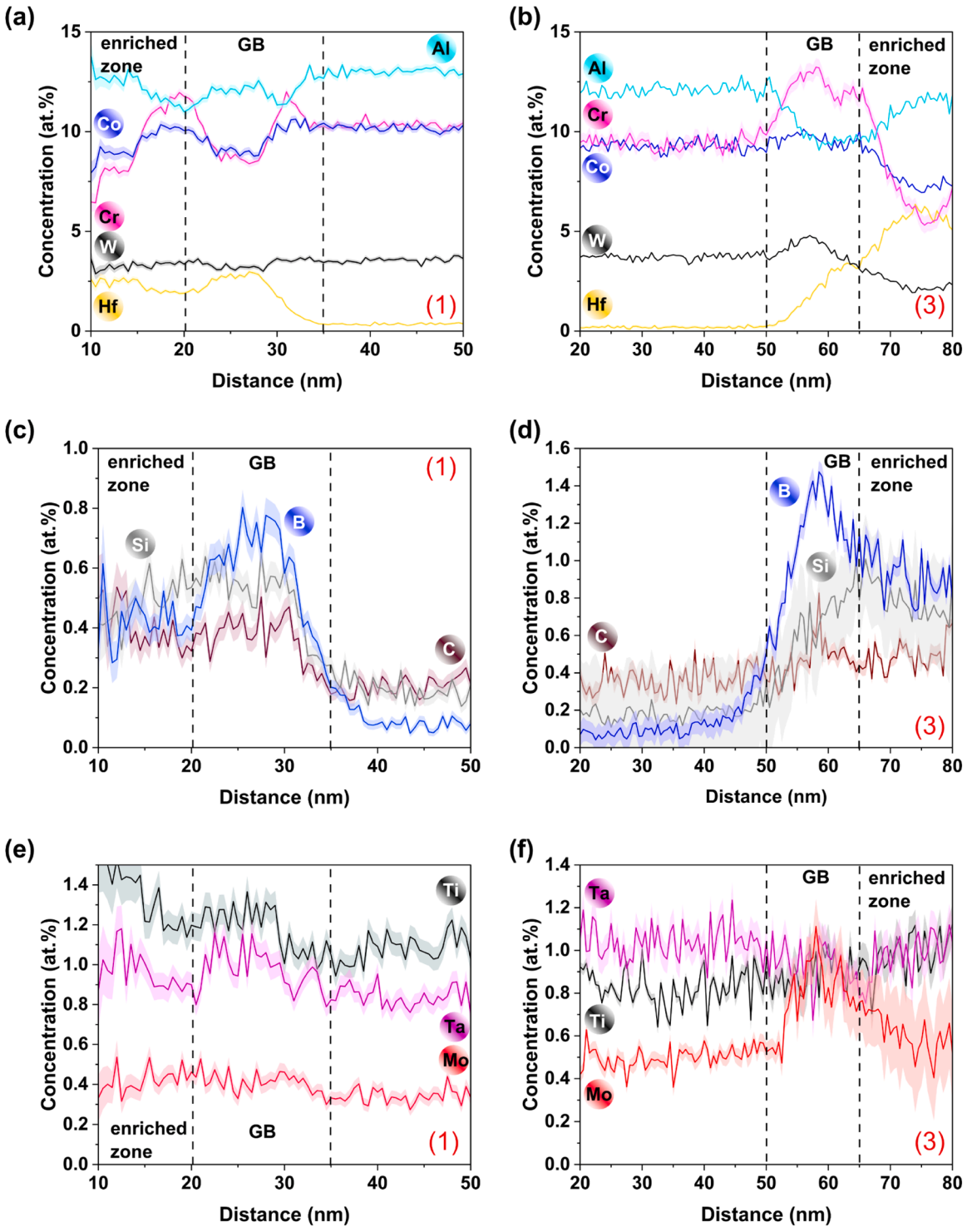

Fig. 10. 1D composition profiles across GBs for samples manufactured with (a, c, e) 5 mm stripe width and (b, d, f) 0.2 mm stripe width. (a, b) Aluminum, cobalt, chromium, tungsten and hafnium. (c, d) Carbon, boron and silicon. (e, f) Molybdenum, tantalum and titanium. The numbers (1 and 3) in each figure correspond to the arrows in Fig. 9(a, c) across which 1D composition profiles were obtained. Error bars are shown as lines with filled color and correspond to the 2σ error.

orientation can be beneficial and can significantly minimize solidification cracking [16,50]. This is because of the lower misorientation between the solidifying structures that promotes attractive GBs instead of repulsive GBs according to the RDG model [42]. It can be inferred from the model and this study that HAGBs are prone to segregation and formation of liquid films at lower temperatures than low LAGBs. The tensile thermal stress acting on the liquid film can lead to a higher cracking susceptibility for HAGB. Therefore, minimizing HAGB and increasing LAGB, i.e. having grains oriented nearly parallel to the building direction (<100> texture), is beneficial for minimizing solidification cracking. Naturally, this leads to columnar anisotropic microstructure at the end.

Segregations in the inter-dendritic regions can be modified, based on the misorientation between cellular structures. The increased Hf and B segregation in the GB of the short stripe width sample is due to a higher fraction of these elements being pushed into the terminal liquid [51].

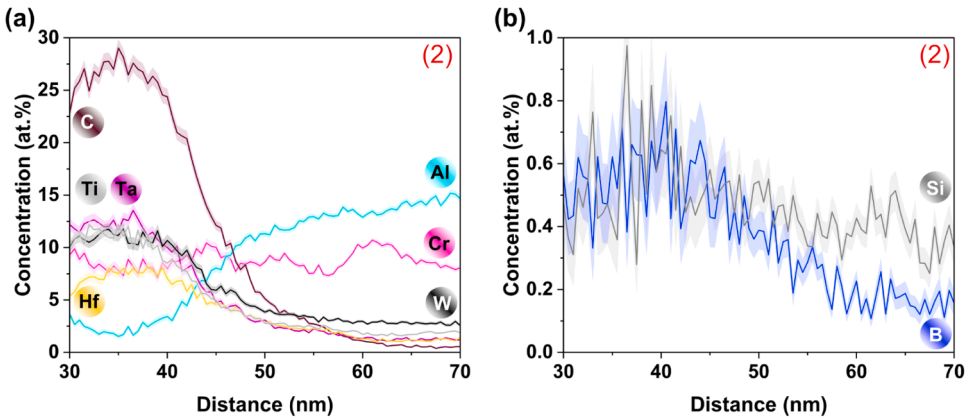

Fig. 11. 1D composition profile across the carbide/matrix interface indicated by arrow 2 in Fig. 9a (a) Carbon, tantalum, aluminum, chromium, hafnium and tungsten. (b) Boron and silicon.

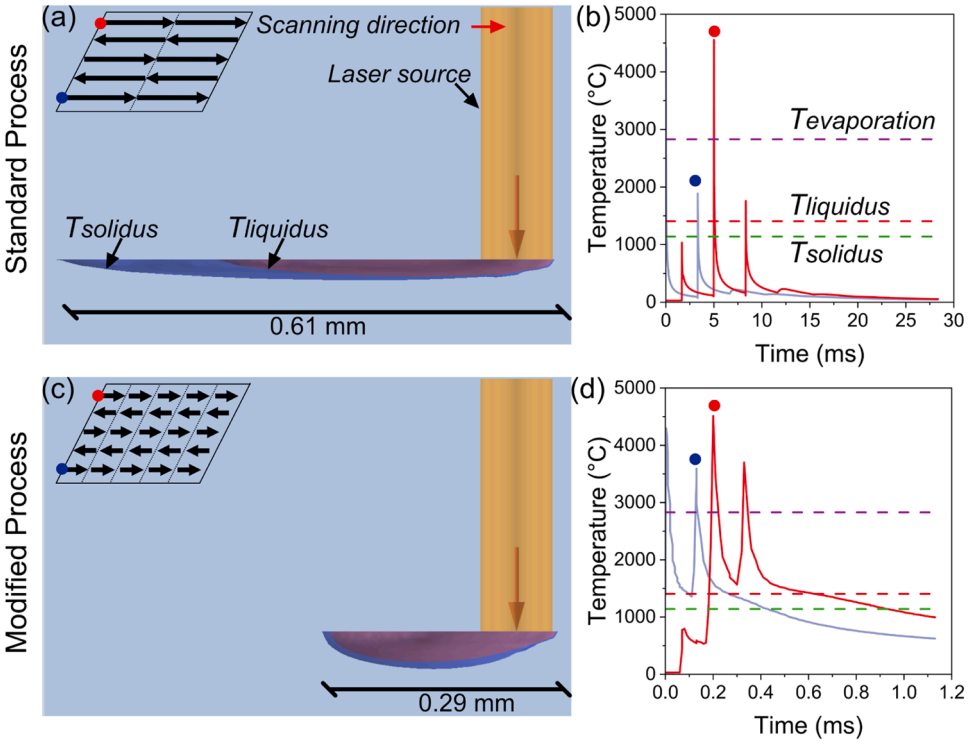

Fig. 12. Simulation showing the melt pool and mushy zone for the (a) standard process (5 mm stripe width) and (c) the modified process (0.2 mm stripe width). Temperature profiles obtained from two probe positions indicated by red and blue dots are shown in (b) standard process and (d) modified process. The simulation was done using the Additive Manufacturing Module in ThermoCalc 2024a. The TCNI12 database was used for calculating the Scheil solidification curves. $T_{evaporation}$ = 2830 °C, $T_{liquidus}$ = 1405 °C, $T_{solidus}$ = 1140 °C.

Table 3
Summary of results indicating the impact of stripe width.

Stripe width	Crack density	Melt pool depth	Mushy zone length	Residual stress*	Dislocation density
mm	mm/mm^2	μm	mm	MPa	10^{14} m^{-2}
5	0.62	53	0.6	842	3.7
2.5	1.11	50	0.95	776	3.9
1	1.71	45	1.06	690	4.8
0.7	0.98	44	0.77	842	5.8
0.5	0.72	41	0.56	875	8.5
0.2	0.33	38	0.29	647	4.8

* Average residual stress in BD

Additionally, the 0.2 mm stripe width also has a higher degree of re-melting than the 5 mm stripe width as the stripe overlap is fixed at 0.12 mm. This re-melting possibly also leads to the solute re-distribution which is likely the reason for the increased segregations observed in the 0.2 mm stripe width. Furthermore, the 5 mm stripe width sample had MC-type carbide near the GB. The lower GB segregation observed is because of the preferential partitioning of Hf and B to the carbide. It could be inferred that there can possibly be higher Hf segregation in the 0.2 mm stripe width that backfills and minimizes solidification cracking. Additionally, the GB misorientation could have also had an impact on the segregation. This will be subject of further studies.

Reducing the stripe width from the standard 5 mm to 0.2 mm led to a 23 % decrease in residual stress (Fig. 8 and Table 3). However, high residual stress (~850 MPa) were found for the 0.7 and 0.5 mm stripe

width. First, the residual stress behavior can be correlated to the solidification cracking. One hypothesis is that increased solidification cracking can lead to stress relaxation. This is observed as the stripe width is reduced from 5 to 2.5 mm. This hypothesis is not valid for the short stripe width of 0.2 mm. The stress relaxation mechanism for the short stripe width is due to the increased re-melting as the stripe overlap was fixed at 0.12 mm. Re-melting has also been shown by Pant *et al.* to lead to a 25 % decrease in residual stresses for IN718. But with CM247LC there is a possible mechanism of solidification cracking also influencing residual stresses. Perhaps, a topic of further study would be to study the impact of re-melting with a double exposure strategy for understanding residual stress development in CM247LC.

It is also important to mention that the type of microstructure (columnar or equiaxed) and the crystallographic texture could accommodate stress differently. The presence of high dislocation density has been reported in as-built conditions for CM247LC and other high γ' Ni-base superalloys [52,53]. The KAM (GND density) was similar, however, there were some differences observed in ECCI. It was observed that the differences in residual stress can be correlated with the dislocation densities measured from ECCI. For example, a 5 mm stripe width with an average stress of 842 MPa had a dislocation density of 3.7×10^{14} m^{-2}. On the other hand, the 0.2 mm stripe width had a stress of 647 MPa and a dislocation density of 4.8×10^{14} m^{-2}. Also, the variations in the stresses with different stripe widths can be explained based on dislocation densities measured using ECCI. According to the authors, the limitation of ECCI could be the measurement of GNDs at the cell walls. In the presence of a dense dislocation network, it is difficult to resolve the dislocations and they all appear as bright features in ECCI. Therefore, the authors believe that the dislocation density values presented are primarily SSDs with minor contributions from GNDs. From our study, it can be inferred that columnar cellular structures could be better than equiaxed cellular structures for accommodating residual stress, as more dislocations are accumulated.

The sharp increase in the $< 100 >$ crystallographic texture along the BD with the reduction in stripe width can be utilized to tailor microstructures. Fig. 13 shows a large area EBSD map obtained from a cube built with a 0.2 mm stripe width, however, the text CAM^2 was built with the 5 mm stripe width. The CAM^2 seems to have finer grains with different crystallographic orientations, however, the background has a strong $< 100 >$ crystallographic texture. Such microstructure tailoring can be attractive for non-weldable Ni-base superalloys such as CM247LC. This microstructure can be compared with the microstructures obtained through directionally solidified (DS) casting. DS microstructures have been known to have superior creep life [54,55] and have been utilized for manufacturing turbine blades. In this study, it is demonstrated that DS-like microstructures can be obtained in PBF-LB with short stripe widths which would potentially lead to improved creep properties. Also, it was shown that the short stripe width also has lower solidification cracking and residual stresses.

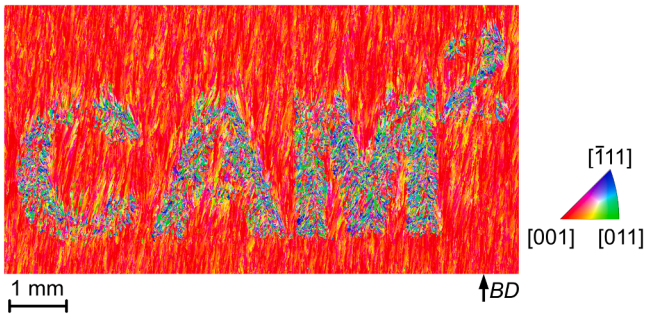

Fig. 13. EBSD orientation maps in IPF representation The orientation map is shown along build direction (BD) and the IPF coloring is along the BD. The text 'CAM^2' utilized 5 mm stripe width process and the remainder of the sample used the 0.2 mm stripe width process.

We conclude that the short stripe width has an increased cracking resistance (both solidification and possibly strain age cracking). With the added benefit of site-specific tailoring, it could be possible to employ the short stripe width process near stress concentrators to reduce strain age cracking that can occur during post-processing heat treatments [15,22].

5. Conclusions

The following are the key findings from the study:

- The reduction in stripe width from 5 to 0.2 mm led to an exponential reduction in melt pool depth from 53 to 38 μm. However, the crack density (indicative of solidification cracking) increased from 0.62 to 1.71 mm/mm^2 as the stripe width was decreased from 5 to 1 mm, this was followed by a sharp decrease of crack density to 0.33 mm/mm^2 for stripe width of 0.2 mm.
- The variation in crack density across the stripe width range is a combined effect of the changes in the solidification structure, microstructure, and mushy zone. The microstructure becomes columnar with an increase in the $< 100 >$ crystallographic texture as the stripe width is reduced from 5 to 0.2 mm which is attributed to the reduction in melt pool depth that promotes epitaxial growth. This solely does not influence the cracking behavior, however, the mushy zone length (from the simulations) provides valuable insight. It is observed that a shorter mushy zone length leads to a decreased solidification cracking which is in accordance with the literature.
- APT revealed that there was an increased GB segregation of Hf and B in the 0.2 mm stripe width in comparison to the 5 mm stripe width. This is caused by re-melting (due to stripe overlap) in the process with 0.2 mm stripe width, which would have caused solute redistribution.
- The average residual stress in the build direction decreased from 842 MPa to 690 MPa as the stripe width reduced from 5 to 1 mm. However, there was a sharp increase of the stresses to 842 and 875 MPa for stripe widths of 0.7 and 0.5 mm, respectively. Here, it can be inferred that the solidification cracking acts as a stress relief mechanism. On the other hand, residual stress of 647 MPa was obtained for the 0.2 mm stripe width likely caused by the re-melting acting as a stress relief mechanism.

Finally, we would like to mention that this study is the first of its kind to explore the impact of stripe width on solidification cracking and residual stresses for such difficult-to-process materials. Further studies would be required to explain some of the mechanisms observed in our study.

CRediT authorship contribution statement

Ahmed Fardan: Writing – original draft, Visualization, Investigation, Conceptualization. **Andrea Fazi:** Writing – review & editing, Visualization, Investigation. **Jakob Schröder:** Writing – review & editing, Visualization, Investigation. **Tatiana Mishurova:** Writing – review & editing, Visualization, Investigation. **Tobias Deckers:** Writing – review & editing, Visualization. **Giovanni Bruno:** Writing – review & editing. **Mattias Thuvander:** Writing – review & editing, Investigation. **Andreas Markström:** Writing – review & editing. **Håkan Brodin:** Writing – review & editing, Supervision, Conceptualization. **Eduard Hryha:** Writing – review & editing, Supervision, Funding acquisition, Conceptualization.

Declaration of Competing Interest

The authors declare that they have no known competing financial interests or personal relationships that could have appeared to influence the work reported in this paper.

Acknowledgements

This work has been performed in the framework of MAGDA (Materials for green hydrogen fueled gas turbines through additive manufacturing) project and the Centre for Additive Manufacturing – Metal (CAM^2), both supported by Swedish Governmental Agency for Innovation Systems (Vinnova). The APT investigations were carried out Chalmers Material Analysis Laboratory (CMAL) at Chalmers University of Technology. The authors thanks X-ray core Lab at HZB (Berlin, Germany) for the access to X-ray diffraction facility.

Appendix A. Supporting information

Supplementary data associated with this article can be found in the online version at doi:10.1016/j.addma.2025.104672.

Data availability

Data will be made available on request.

References

[1] W.E. Frazier, Metal additive manufacturing: a review, J. Mater. Eng. Perform. 23 (2014) 1917–1928, https://doi.org/10.1007/s11665-014-0958-z.
[2] H. Jia, H. Sun, H. Wang, Y. Wu, H. Wang, Scanning strategy in selective laser melting (SLM): a review, Int. J. Adv. Manuf. Technol. 113 (2021) 2413–2435, https://doi.org/10.1007/s00170-021-06810-3.
[3] S. Chowdhury, N. Yadaiah, C. Prakash, S. Ramakrishna, S. Dixit, L.R. Gupta, D. Buddhi, Laser powder bed fusion: a state-of-the-art review of the technology, materials, properties & defects, and numerical modelling, J. Mater. Res. Technol. 20 (2022) 2109–2172, https://doi.org/10.1016/j.jmrt.2022.07.121.
[4] G.M. Volpato, U. Tetzlaff, M.C. Fredel, A comprehensive literature review on laser powder bed fusion of Inconel superalloys, Addit. Manuf. 55 (2022) 102871, https://doi.org/10.1016/j.addma.2022.102871.
[5] O. Adegoke, J. Andersson, H. Brodin, R. Pederson, Review of laser powder bed fusion of gamma-prime-strengthened nickel-based superalloys, Metals 10 (2020) 1–26, https://doi.org/10.3390/met10080996.
[6] J.N. DuPont, J.C. Lippold, S.D. Kiser, Welding Metallurgy and Weldability of Nickel-Base Alloys, Wiley Online Library, 2009, https://doi.org/10.1002/9780470500262.
[7] J. Xu, P. Kontis, R.L. Peng, J. Moverare, Modelling of additive manufacturability of nickel-based superalloys for laser powder bed fusion, Acta Mater. 240 (2022) 118307, https://doi.org/10.1016/j.actamat.2022.118307.
[8] D. Grange, J.D. Bartout, B. Macquaire, C. Colin, Processing a non-weldable nickel-base superalloy by Selective Laser Melting: role of the shape and size of the melt pools on solidification cracking, Materialia 12 (2020), https://doi.org/10.1016/j.mtla.2020.100686.
[9] P. Kontis, E. Chauvet, Z. Peng, J. He, A.K. da Silva, D. Raabe, C. Tassin, J. J. Blandin, S. Abed, R. Dendievel, B. Gault, G. Martin, Atomic-scale grain boundary engineering to overcome hot-cracking in additively-manufactured superalloys, Acta Mater. 177 (2019) 209–221, https://doi.org/10.1016/j.actamat.2019.07.041.
[10] A. Després, S. Antonov, C. Mayer, C. Tassin, M. Veron, J.J. Blandin, P. Kontis, G. Martin, On the role of boron, carbon and zirconium on hot cracking and creep resistance of an additively manufactured polycrystalline superalloy, Materialia 19 (2021), https://doi.org/10.1016/j.mtla.2021.101193.
[11] K. Lindgren, F. Schulz, H. Gruber, A. Markström, E. Hryha, On the role of Zr and B addition on solidification cracking of IN738LC produced by laser powder bed fusion, Materialia 26 (2022) 101609, https://doi.org/10.1016/j.mtla.2022.101609.
[12] L. Liu, D. Wang, G. Deng, Z. Liu, C. Tan, X. Zhou, C. Han, R. Jiang, Y. Yang, Crack inhibition to enhance strength-ductility of CM247LC alloy fabricated by laser powder bed fusion, Mater. Sci. Eng. A. 875 (2023) 145114, https://doi.org/10.1016/j.msea.2023.145114.
[13] B. Kumar, S. Sahu, D. Srinivasan, N.J. Balila, Influence of heat input on solidification cracking in additively manufactured CM247LC Ni-based Superalloy, Metall. Mater. Trans. A. (2022), https://doi.org/10.1007/s11661-023-07027-7.
[14] M. Gerstgrasser, M. Cloots, J. Stirnimann, K. Wegener, Residual stress reduction of LPBF-processed CM247LC samples via multi laser beam strategies, Int. J. Adv. Manuf. Technol. 117 (2021) 2093–2103, https://doi.org/10.1007/s00170-021-07083-6.
[15] J.H. Boswell, D. Clark, W. Li, M.M. Attallah, Cracking during thermal post-processing of laser powder bed fabricated CM247LC Ni-superalloy, Mater. Des. 174 (2019) 107793, https://doi.org/10.1016/j.matdes.2019.107793.
[16] A. Fardan, A. Fazi, R.L. Peng, T. Mishurova, M. Thuvander, G. Bruno, H. Brodin, E. Hryha, Fine-tuning melt pools and microstructures: taming cracks in powder bed fusion – laser beam of a non-weldable Ni-base superalloy, Materialia (2024) 102059, https://doi.org/10.1016/j.mtla.2024.102059.
[17] J.N. Ghoussoub, Y.T. Tang, C. Panwisawas, A. Németh, R.C. Reed, On the Influence of Alloy Chemistry and Processing Conditions on Additive Manufacturability of Ni-Based Superalloys, Springer International Publishing, 2020, https://doi.org/10.1007/978-3-030-51834-9_15.
[18] J. Xu, H. Gruber, R.L. Peng, J. Moverare, A novel γ′-strengthened nickel-based superalloy for laser powder bed fusion, Materials 13 (2020) 1–12, https://doi.org/10.3390/ma13214930.
[19] M.C. Lam, S.C.V. Lim, H. Song, Y. Zhu, X. Wu, A. Huang, Scanning strategy induced cracking and anisotropic weakening in grain texture of additively manufactured superalloys, Addit. Manuf. 52 (2022) 102660, https://doi.org/10.1016/j.addma.2022.102660.
[20] K. Prasad, M. Obana, Y. Ishii, A. Ito, S. Torizuka, The effect of laser scanning strategies on the microstructure, texture and crystallography of grains exhibiting hot cracks in additively manufactured Hastelloy X, Mech. Mater. 157 (2021), https://doi.org/10.1016/j.mechmat.2021.103816.
[21] M.A.L. Phan, O. Dew, I. Todd, Predictive process diagram for parameters selection in laser powder bed fusion to achieve high-density and low-cracking built parts, Addit. Manuf. 85 (2024) 104145, https://doi.org/10.1016/j.addma.2024.104145.
[22] H. Hilal, R. Lancaster, D. Stapleton, G. Baxter, Investigating the influence of process parameters on the structural integrity of an additively manufactured nickel-based superalloy, Metals 9 (2019), https://doi.org/10.3390/met9111191.
[23] A. Soltani-Tehrani, M.S. Yasin, S. Shao, N. Shamsaei, Effects of stripe width on the porosity and mechanical performance of additively manufactured Ti-6Al-4V parts, Proc. 32nd Solid Free. Fabr. Symp. (2021) 1061–1075.
[24] C. Högman, The Effect of Stripe Width, Stripe Overlap, Gas Flow, and Scan Angle on Process Stability in Laser Powder Bed Fusion (L-PBF), Karlstad University, 2021. ⟨https://www.diva-portal.org/smash/record.jsf?pid=diva2%3A1601112&dswid= 9022⟩.
[25] K. Peng, R. Duan, Z. Liu, X. Lv, Q. Li, F. Zhao, B. Wei, B. Nong, S. Wei, Cracking behavior of rené 104 nickel-based superalloy prepared by selective laser melting using different scanning strategies, Materials 13 (2020), https://doi.org/10.3390/ma13092149.
[26] R. Magana-Carranza, C.J. Sutcliffe, E.A. Patterson, The effect of processing parameters and material properties on residual forces induced in Laser Powder Bed Fusion (L-PBF), Addit. Manuf. 46 (2021) 102192, https://doi.org/10.1016/j.addma.2021.102192.
[27] A.B. Freemelt, 2024, Electron beam powder bed fusion processing of pure tungsten, (2024). ⟨https://freemelt.com/knowledge/electron-beam-powder-bed-fusion-processing-of-pure-tungsten/?lang=sv⟩(Accessed March 24, 2024).
[28] L. ZeyuElectron beam powder bed fusion of Nitinol: A development from production process window towards delicate structures, KTH, Production engineering, 2023.
[29] L.N. Carter, M.M. Attallah, R.C. Reed, Laser powder bed fabrication of nickel-base superalloys: Influence of parameters; characterisation, quantification and mitigation of cracking, Proc. Int. Symp. Superalloys. (2012) 577–586, https://doi.org/10.7449/2012/superalloys_2012_577_586.
[30] J. Schindelin, I. Arganda-Carreras, E. Frise, V. Kaynig, M. Longair, T. Pietzsch, S. Preibisch, C. Rueden, S. Saalfeld, B. Schmid, J.-Y. Tinevez, D.J. White, V. Hartenstein, K. Eliceiri, P. Tomancak, A. Cardona, Fiji: an open-source platform for biological-image analysis, Nat. Methods 9 (2012) 676–682, https://doi.org/10.1038/nmeth.2019.
[31] F. Bachmann, R. Hielscher, H. Schaeben, Texture analysis with MTEX–free and open source software toolbox, Solid State Phenom. 160 (2010) 294–306, https://doi.org/10.4028/www.scientific.net/SSP.160.63.
[32] S. Zaefferer, N.N. Elhami, Theory and application of electron channelling contrast imaging under controlled diffraction conditions, Acta Mater. 75 (2014) 20–50, https://doi.org/10.1016/j.actamat.2014.04.018.
[33] I. Arganda-Carreras, V. Kaynig, C. Rueden, K.W. Eliceiri, J. Schindelin, A. Cardona, H. Sebastian Seung, Trainable Weka Segmentation: a machine learning tool for microscopy pixel classification, Bioinformatics 33 (2017) 2424–2426, https://doi.org/10.1093/bioinformatics/btx180.
[34] I. Gutierrez-Urrutia, S. Zaefferer, D. Raabe, Coupling of electron channeling with EBSD: Toward the quantitative characterization of deformation structures in the sem, Jom 65 (2013) 1229–1236, https://doi.org/10.1007/s11837-013-0678-0.
[35] K. Thompson, D. Lawrence, D.J. Larson, J.D. Olson, T.F. Kelly, B. Gorman, In situ site-specific specimen preparation for atom probe tomography, Ultramicroscopy 107 (2007) 131–139, https://doi.org/10.1016/j.ultramic.2006.06.008.
[36] D. Apel, M. Genzel, M. Meixner, M. Boin, M. Klaus, C. Genzel, EDDIDAT: a graphical user interface for the analysis of energy-dispersive diffraction data, J. Appl. Crystallogr. 53 (2020) 1130–1137, https://doi.org/10.1107/S1600576720005506.
[37] T. Gnäupel-Herold, ISODEC: software for calculating diffraction elastic constants, J. Appl. Crystallogr. 45 (2012) 573–574, https://doi.org/10.1107/S0021889812014252.
[38] S. Ma, P. Rangaswamy, B.S. Majumdar, Microstress evolution during in situ loading of a superalloy containing high volume fraction of γ′ phase, Scr. Mater. 48 (2003) 525–530, https://doi.org/10.1016/S1359-6462(02)00504-3.
[39] Thermo-Calc Software AB, Additive Manufacturing (AM) Module User Guide, 2024. ⟨https://thermocalc.com/wp-content/uploads/Documentation/Getting_Started/additive-manufacturing-module-getting-started-guide.pdf⟩.
[40] J. Schröder, A. Evans, V. Luzin, G. Abreu Faria, S. Degener, E. Polatidis, J. Čapek, A. Kromm, G. Dovzhenko, G. Bruno, J. Keckes, Texture-based residual stress analysis of laser powder bed fused Inconel 718 parts, J. Appl. Crystallogr. 56 (2023) 1076–1090, https://doi.org/10.1107/S1600576723004855.
[41] A. Hariharan, L. Lu, J. Risse, A. Kostka, B. Gault, E.A. Jägle, D. Raabe, Misorientation-dependent solute enrichment at interfaces and its contribution to defect formation mechanisms during laser additive manufacturing of superalloys,

Phys. Rev. Mater. 3 (2019) 123602, https://doi.org/10.1103/PhysRevMaterials.3.123602.
[42] M. Rappaz, J.M. Drezet, M. Gremaud, A new hot-tearing criterion, Metall. Mater. Trans. A Phys. Metall. Mater. Sci. 30 (1999) 449–455, https://doi.org/10.1007/s11661-999-0334-z.
[43] C. Guo, G. Li, S. Li, X. Hu, H. Lu, X. Li, Z. Xu, Y. Chen, Q. Li, J. Lu, Q. Zhu, Additive manufacturing of Ni-based superalloys: residual stress, mechanisms of crack formation and strategies for crack inhibition, Nano Mater. Sci. 5 (2023) 53–77, https://doi.org/10.1016/j.nanoms.2022.08.001.
[44] T.W. ClyneThe Influence of Composition on Solidification Cracking Susceptibility in Binary Alloy Systems, (1981).
[45] S. Kou, Solidification cracking susceptibility associated with a teardrop-shaped weld pool, Sci. Technol. Weld. Join. 26 (2021) 341–347, https://doi.org/10.1080/13621718.2021.1910179.
[46] S. Kou, Weld metal solidification I: grain structure, Weld. Metall. (2002) 170–198, https://doi.org/10.1002/0471434027.ch7.
[47] T. DebRoy, H.L. Wei, J.S. Zuback, T. Mukherjee, J.W. Elmer, J.O. Milewski, A. M. Beese, A. Wilson-Heid, A. De, W. Zhang, Additive manufacturing of metallic components – Process, structure and properties, Prog. Mater. Sci. 92 (2018) 112–224, https://doi.org/10.1016/j.pmatsci.2017.10.001.
[48] O. Gokcekaya, T. Ishimoto, S. Hibino, J. Yasutomi, T. Narushima, T. Nakano, Unique crystallographic texture formation in Inconel 718 by laser powder bed fusion and its effect on mechanical anisotropy, Acta Mater. 212 (2021) 116876, https://doi.org/10.1016/j.actamat.2021.116876.
[49] S. Kou. Welding Metallurgy, second ed., Wiley, 2003. ⟨https://search.ebscohost.com/login.aspx?direct=true&db=cat07470a&AN=clc.ad7629d2.db86.42f7.a711.34443afdb233&site=eds-live&scope=site&authtype=guest&custid=s3911979&groupid=main&profile=eds⟩.
[50] E. Chauvet, P. Kontis, E.A. Jägle, B. Gault, D. Raabe, C. Tassin, J.J. Blandin, R. Dendievel, B. Vayre, S. Abed, G. Martin, Hot cracking mechanism affecting a non-weldable Ni-based superalloy produced by selective electron Beam Melting, Acta Mater. 142 (2018) 82–94, https://doi.org/10.1016/j.actamat.2017.09.047.
[51] P. Hu, Z. Liu, M. Chen, Y. Li, X. Qi, J. Xie, Reducing cracking sensitivity of CM247LC processed via laser powder bed fusion through composition modification, J. Mater. Res. Technol. 29 (2024) 3074–3088, https://doi.org/10.1016/j.jmrt.2024.02.082.
[52] X. Wang, L.N. Carter, B. Pang, M.M. Attallah, M.H. Loretto, Microstructure and yield strength of SLM-fabricated CM247LC Ni-Superalloy, Acta Mater. 128 (2017) 87–95, https://doi.org/10.1016/j.actamat.2017.02.007.
[53] V.D. Divya, R. Muñoz-Moreno, O.M.D.M. Messé, J.S. Barnard, S. Baker, T. Illston, H.J. Stone, Microstructure of selective laser melted CM247LC nickel-based superalloy and its evolution through heat treatment, Mater. Charact. 114 (2016) 62–74, https://doi.org/10.1016/j.matchar.2016.02.004.
[54] G.L. Erickson, K. Harris, R.E. Schwer, Directionally solidified DS CM 247 LC—optimized mechanical properties resulting from extensive γ′ solutioning, Turbo Expo. Power Land, Sea, Air 79412 (1985). V004T11A006.
[55] M. Ramsperger, S. Eichler, Electron beam based additive manufacturing of alloy 247 for turbine engine application: from research towards industrialization, Metall. Mater. Trans. A Phys. Metall. Mater. Sci. 54 (2023) 1730–1743, https://doi.org/10.1007/s11661-022-06955-0.